AGU PUBLICATIONS

JGR

Journal of Geophysical Research: Oceans

RESEARCH ARTICLE

10.1002/2017JC013408

Special Section:
The Southern Ocean Carbon and Climate Observations and Modeling (SOCCOM) Project: Technologies, Methods, and Early Results

Correlation Lengths for Estimating the Large-Scale Carbon and Heat Content of the Southern Ocean

M. R. Mazloff[1], B. D. Cornuelle[1], S. T. Gille[1], and A. Verdy[1]

[1]Scripps Institution of Oceanography, University of California San Diego, La Jolla, CA, USA

Abstract The spatial correlation scales of oceanic dissolved inorganic carbon, heat content, and carbon and heat exchanges with the atmosphere are estimated from a realistic numerical simulation of the Southern Ocean. Biases in the model are assessed by comparing the simulated sea surface height and temperature scales to those derived from optimally interpolated satellite measurements. While these products do not resolve all ocean scales, they are representative of the climate scale variability we aim to estimate. Results show that constraining the carbon and heat inventory between 35°S and 70°S on time-scales longer than 90 days requires approximately 100 optimally spaced measurement platforms: approximately one platform every 20° longitude by 6° latitude. Carbon flux has slightly longer zonal scales, and requires a coverage of approximately 30° by 6°. Heat flux has much longer scales, and thus a platform distribution of approximately 90° by 10° would be sufficient. Fluxes, however, have significant subseasonal variability. For all fields, and especially fluxes, sustained measurements in time are required to prevent aliasing of the eddy signals into the longer climate scale signals. Our results imply a minimum of 100 biogeochemical-Argo floats are required to monitor the Southern Ocean carbon and heat content and air-sea exchanges on time-scales longer than 90 days. However, an estimate of formal mapping error using the current Argo array implies that in practice even an array of 600 floats (a nominal float density of about 1 every 7° longitude by 3° latitude) will result in nonnegligible uncertainty in estimating climate signals.

Key Points:
- Spatial correlation scales of air-sea fluxes and content of both carbon and heat are estimated to inform observational coverage requirements
- Over 100 biogeochemical-Argo floats are required to monitor the Southern Ocean carbon and heat content on time-scales longer than 90 days
- Though fluxes have longer spatial correlation scales, they have significant temporal variance at periods less than 90 days

Correspondence to:
M. R. Mazloff,
mmazloff@ucsd.edu

Citation:
Mazloff, M. R., Cornuelle, B. D., Gille, S. T., & Verdy, A. (2018). Correlation lengths for estimating the large-scale carbon and heat content of the Southern Ocean. *Journal of Geophysical Research: Oceans*, *123*. https://doi.org/10.1002/2017JC013408

Received 1 SEP 2017
Accepted 3 JAN 2018
Accepted article online 9 JAN 2018

© 2018. American Geophysical Union. All Rights Reserved.

1. Introduction

Quantifying the oceanic dissolved inorganic carbon and oceanic heat content as well as the carbon and heat exchanges between the atmosphere and ocean is a central objective in chemical and physical oceanography. The oceans are vast: although satellite remote sensing offers a global view of the ocean surface, interior oceanic properties, and exchanges between the atmosphere and ocean are difficult to infer from remote sensing. Technologies that enhance our observing system are rapidly advancing. The last decade saw a proliferation of floats equipped with temperature and salinity sensors (e.g., Riser et al., 2016), and the next decade promises to enhance this capability using biogeochemical sensors (Johnson & Claustre, 2016). Nevertheless, ocean measurements are sparse and expensive, and we aim to maximize the value of our resources. This paper takes a first step in determining observational coverage needs by estimating the spatial correlation scales of air-sea exchange, and ocean inventory of carbon and heat for time-scales of 90 days and longer, and space scales of 1,000 km and longer. For the purposes of this analysis, higher frequency and higher wavenumber variability is treated as noise, although we recognize that they can represent a significant fraction of the total variability.

Correlation scales inform requirements for an observational system able to address climate problems. Temporal correlation scales can be inferred from time series measurements from moorings or gliders (e.g., Garrett & Munk, 1975; Swart et al., 2015). Temporal correlations have also been inferred from shipboard in situ measurements (e.g., Jones et al., 2012). Spatial correlations, averaged in time between mooring sites, have been computed for overlapping time series (e.g., Bretherton et al., 1976) at a few locations, but to do this globally from observations requires coverage that is currently only attainable from satellite measurements.

Previous work has analyzed spatial autocorrelations by calculating the correlation of a time-invariant property with itself at given spatial lags, averaged over a geographic region. For example, Purkey and Johnson (2010) estimated autocorrelations of temperature trends. And Jones et al. (2012) estimated a global mean

partial pressure of carbon dioxide (pCO_2) autocorrelation scale of 400 ± 250 km, with a range of 50–3,000 km depending on the dynamics of the region. They found CO_2 flux autocorrelation scales to be shorter (200 ± 150 km). These spatial autocorrelation scales are useful for determining the length scale where spatial anomalies begin to repeat. Results can be difficult to interpret; however, as the continuum of ocean scales often makes it difficult to isolate the anomaly scales one wishes to estimate.

In contrast, analyzing the correlation between two locations reveals the spatial extent of property variations in time, showing the representativeness in space of a measurement or time series. Correlation lengths imply the scales of spatial smoothness in property variability, but not in the mean state. For example, a sharp front could correspond to a change in mean properties over a 20 km scale, but the variability might nonetheless show a 1,000 km correlation scale. This implies temporal changes in the property, which includes effects from instabilities and meanders of the front, occur in phase over a region on the scale of 1,000 km. In this way spatial correlation scales give a region of impact of climate observations.

As stated, however, correlation scales are currently only observable by satellite. The fact that carbon and heat content and air-sea exchanges covary with some variables that are observable from space has been exploited. Noteworthy efforts include the use of Multi-Parameter Linear regression (Chierici et al., 2012) and neural network methods (Landschutzer et al., 2014). Both these efforts also relied on model solutions to derive their mapping algorithms and products. These efforts, however, did not attempt to determine or validate correlation length scales in their derived products.

Here we use a different derived product, a Biogeochemical Southern Ocean State Estimate (B-SOSE, Verdy & Mazloff, 2017), to estimate spatial correlation scales. This is the first attempt, we are aware of to use a numerical model solution to determine these scales. There are a number of caveats in making such a calculation. The most significant is that the state estimate does not resolve high-frequency and high-wavenumber dynamics (i.e., scales less than 10 days and 1,000 km are poorly represented). Our aim is to provide guidance for quantifying properties on climate scales; however, an observing system must be cognizant of aliased high-frequency and high-wavenumber dynamics. Analysis of observational time series continues to inform temporal sampling requirements. For example, recent work by Monteiro et al. (2015) finds that sampling intervals for air-sea CO_2 flux should be no longer than 2 days. Here we assess spatial sampling requirements.

Our assessment relies on the fundamental assumption in ocean modeling that low-wavenumbers can be accurately simulated even if high-wavenumbers are unresolved. This is accomplished by exploiting skillful parameterizations for the effects of mesoscale, submesoscale, and wave dynamics. Model solutions are not simply providing a truncated spectrum of ocean variability; biases are present in the large-scale model solution due to resolution and other approximations. In this work, we attempt to diagnose and correct for model biases using mapped satellite observations.

We focus on the Southern Ocean for two reasons. First, this is a primary region for water mass upwelling, transformation, and subduction (e.g., Abernathey et al., 2016). Because of this connectivity of the interior ocean with the atmosphere, the Southern Ocean plays a vital role in air-sea exchange, with the capability of releasing or sequestering massive amounts of carbon and heat (Russell et al., 2006). The second reason is intrinsically related: because the interior Southern Ocean is connected to the atmosphere on relatively short timescales, its climate is subject to more rapid change. Thus, deploying an observing system in the Southern Ocean is more pressing than in many other ocean regions.

We aim to provide guidance for deployment of a Southern Ocean observing system to quantify dissolved inorganic carbon content, heat content, and the associated air-sea exchanges. The manuscript is organized as follows: in the next section, we present the model and method for determining spatial correlation length scales. We then assess the model realism by applying the method to the model and to sea surface height (SSH) and sea surface temperature (SST) products from objectively mapped satellite measurements. In section 3, we apply the method to diagnose the spatial correlation length scales of carbon and heat fluxes as well as their inventories within the upper ocean. In section 4, we discuss implications of sensor limitations and of model and product imperfections. We also summarize the results and discuss implications for the Southern Ocean observing system in this final section. For brevity, throughout the remainder of this manuscript, we refer to dissolved inorganic carbon simply as carbon.

2. Methods

2.1. The Biogeochemical-Sea Ice-Ocean State Estimate

The model used is the data-assimilating B-SOSE, which is produced using the machinery developed by the consortium for Estimating the Circulation and Climate of the Ocean (ECCO; http://www.ecco-group.org). The ECCO state estimation machinery have been extensively described in the literature (e.g., Wunsch & Heimbach, 2013). B-SOSE is introduced by Verdy and Mazloff (2017), and thus in this section we give only a brief summary.

B-SOSE uses the MIT global circulation model (MITgcm, Marshall et al., 1997), and includes a coupled sea-ice model (Losch et al., 2010), and biogeochemical model evolved from Galbraith et al. (2010). The isotropic zonal and meridional grid spacing is 1/3° in the zonal direction. However equatorward of 30°S the meridional resolution telescopes out to reach 2.2°N by 1.8°N, which is the northern boundary of the domain. The model uses 52 vertical levels of varying thickness, starting with 4.2 m resolution for the surface layer. Model ability to reproduce the observations is measured with a cost function, $\mathcal{J}$, which is the scalar sum over time and space of weighted squared differences between the dynamical model state and observations. Optimization is sought by iteratively reducing $\mathcal{J}$ by adjusting the model control vector, $\mathbf{u}$, which in the present configuration consists of initial conditions and surface boundary (atmospheric state) conditions. The methodology is that of classical weighted least squares with Lagrange multipliers, but numerically exploiting the existence of an adjoint model produced by algorithmic differentiation (Giering & Kaminski, 1998). The adjoint model calculates the cost function gradients with respect to the controls, $\nabla_{\mathbf{u}}\mathcal{J}$, thereby increasing the efficiency of the quasi-Newton optimization algorithm (Gilbert & Lemaréchal, 1989). When an acceptable misfit is found, the state estimate is determined by running the *free* model forward in time using the adjusted control vector over the entire length of the assimilation window. In that important sense, the state estimate is obtained from a model solution with closed dynamical, thermodynamical, and biogeochemical budgets. This is important for this work as unphysical jumps in the solution would affect the statistics.

We use 3 day average output from the 2008 to 2012 B-SOSE solution, which is available at http://sose.ucsd.edu/BSOSE_iter105_solution.html. Validation of the solution is presented by Verdy and Mazloff (2017) and at http://sose.ucsd.edu/BSOSE_iter105_valid.html. The mean circulation in B-SOSE is illustrated by the vertically integrated transport streamfunction (Figure 1). The primary structure is the Antarctic Circumpolar Current (ACC) separating the subtropical gyres and the subpolar gyres. At several regions of complex topography, the ACC streamlines converge, indicating faster currents. The ACC fronts are denoted by these closely spaced streamlines, and we have made three streamlines bold. The northern bold streamline is a proxy for the northern boundary of the ACC, and in most regions also a proxy for the Subantarctic Front (SAF). Likewise, the most poleward bold streamline denotes the southern ACC boundary and is often representative of the position of the Southern ACC Front (SACCF). The middle bold streamline is a proxy for the position of the Polar Front (PF). The B-SOSE ACC transport is ∼180 Sv, consistent with the 173.3 ± 10.7 Sv estimate of Donohue et al. (2016). The strength of the Ross Gyre is about 20 Sv and the Weddell Gyre about 40 Sv.

2.2. Validation With Sea Surface Height and Temperature

To introduce our methods and validate the model statistics, we compare to an SST product obtained by mapping satellite microwave radiometer observations, hereafter referred to as MWOI (www.remss.com). Figure 2 shows the standard deviation of SST from this product and from B-SOSE. The B-SOSE solution is generally smoother, but the large-scale structures are similar. The root-mean-square standard deviation in the region is 1.53°C for both B-SOSE and the MWOI product. A comparison to an SSH product produced by mapping satellite altimeter observations (AVISO; http://www.aviso.altimetry.fr) reveals that model has similar but smoother structure (not shown). The model SSH variance is muted; however, with the root-mean-square standard deviation in the region being 5.4 cm for B-SOSE and 9.0 cm for the AVISO product. Both the SST and SSH products are smoother than the true ocean, with neither resolving the submesoscale. Infrared SST observations do resolve these scales, but cannot measure in the presence of clouds, which is problematic for quantifying the spatial scales we wish to determine. We have chosen not to use merged infrared and microwave products due to concerns that the merging of high and low-resolution data may introduce artificial high-wavenumber structure.

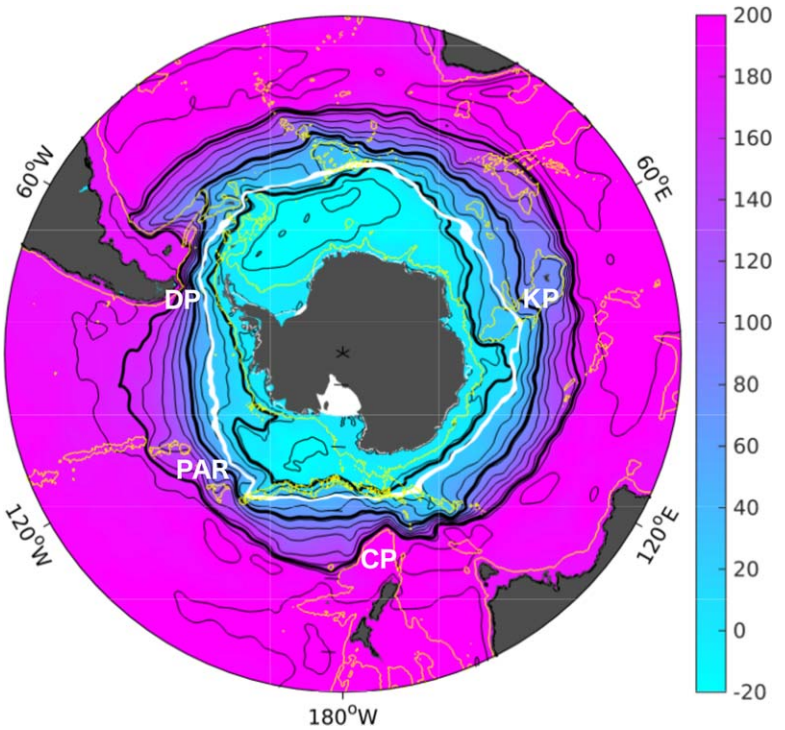

Figure 1. Vertically integrated streamfunction [Sv] averaged over the 2008–2012 B-SOSE solution. Black lines are contours every 20 Sv from −40 to 240 Sv. Additionally, we have drawn bold contours of 5, 75, and 170 Sv transport streamlines. The 5 and 170 Sv denote the boundaries of the ACC, and are also often associated with the positions of the Southern ACC front and the Subantarctic Front, respectively. The 75 Sv streamline between is often associated with the Polar Front position. The white region denotes the mean August ice extent from B-SOSE by filling the area where mean concentration is between 10 and 20%. The yellow contour denotes the 3,000 m bathymetric contour, highlighting the continental shelves, mid-ocean ridges, and several other topographic features. In all future figures these contours are used, though bathymetry is drawn in magenta instead of yellow. Bathymetric features mentioned in the text are labeled: Campbell Plateau (CP), Drake Passage (DP), Kerguelen Plateau (KP), and Pacific-Antarctic Ridge (PAR).

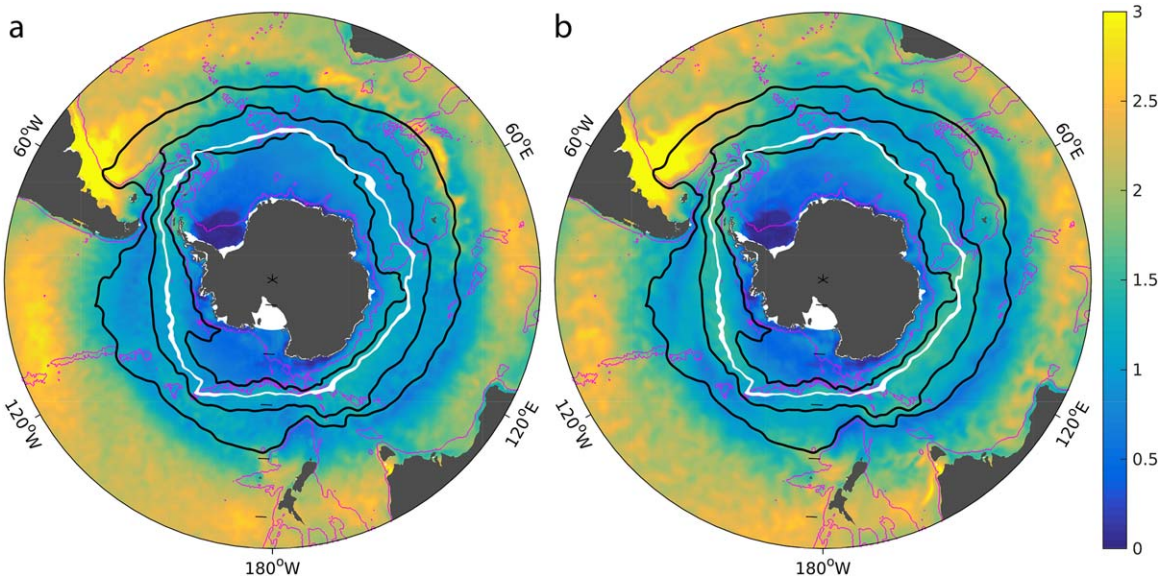

Figure 2. SST standard deviation from (a) MWOI and (b) B-SOSE (°C). As in Figure 1, the black contours are ACC streamlines, the White contour is mean August ice extent, and magenta is the 3,000 m bathymetric contour.

Mapped SST and SSH products resolve mesoscale and larger structures. In an attempt to separate the longer timescale signals, such as the annual cycle, from the mesoscale eddy signals, we calculate a low-pass (i.e., long-period) component using a 90 day running mean. The residual that is orthogonal, and thus uncorrelated, to the low-pass time series becomes the high-pass (i.e., short-period) time series. For SST, the low-pass component is dominant, on average explaining 87% of the variance with a standard deviation of 8% in the MWOI product, and 94 ± 6% in B-SOSE. The high-pass component is nonnegligible in the ACC and the subpolar gyre (not shown), but averaged over the domain it only explains 11 ± 8% in the product and 5 ± 6% in B-SOSE. Considering every point in the domain, the maximum variance explained by the high-pass component is 84% for the MWOI product and 68% for B-SOSE.

For SSH, the short timescale variance is more significant everywhere, and not simply in the fronts and subpolar gyres as was found for SST. Nevertheless, the variance explained by the low-pass component is dominant, explaining 68 ± 17% for the AVISO product and 73 ± 16% for B-SOSE. The high-pass components explain 31 ± 18% for the AVISO product and 27 ± 26% for B-SOSE. For SSH, there are a few confluence regions and topographically complex locations where the high-pass components explain the majority of the variance. The Argentine Shelf is the most notable location where the high-pass components dominate.

For the low and high-pass components, we analyze correlation averaged in time between two locations as follows. For each field considered (i.e., high/low-pass SST/SSH from each product), we normalize the covariance by the local temporal standard deviation in order to determine the correlation. For computational efficiency we evaluate the correlation scales at points separated by 3° longitude and by approximately 1.1° latitude. From 70°S to 35°S we have 3,720 points to evaluate to map spatial correlation scales. We correlate the time series from each of these 3,720 points with the time series at every point from the original grid of the model or the maps (i.e., far greater than 3,720 points). Though we consider the correlation at a subset of points, for each point in the subset the correlations are exact, since they use data from the entire grid.

The individual correlation maps of the field with other locations have significant structure. Typically, the correlation falls off rather quickly with distance from 1.0 to about 0.8, but rather high correlations reaching about 0.7 are found even at substantial distances. Some of these are spurious, but many are due to remote influences. For example, the annual cycle is a dominant mode of variability and will introduce remote correlations. However, determining regional anomalies with respect to the annual cycle is a primary goal and we do not expect an observation can constrain these anomalies 180° of longitude away. To make the problem tractable, we assume that the spatial correlation structure at any point takes the form of a single two-dimensional Gaussian, $e^{(-a_1x^2-a_2xy-a_3y^2)}$, and thus that correlation asymptotes to zero at great distances. We calculate the negative log of the correlation field, $\mathbf{y}$, and least squares fit it to $\mathbf{g}=\mathbf{Ha}$. Here $\mathbf{H}$ is a function of the coordinate system allowing a linearized conversion from the Gaussian parameters, $\mathbf{a}=[a_1+a_2+a_2]$, to $\mathbf{g}$. We solve for $\mathbf{a}$ as follows:

1. Converting into polar coordinates, we discretize the field into 20° sectors. We then search for the closest point in each sector where the correlation falls to 0.8. We use this radius information to develop an a priori guess of the Gaussian parameters, $\mathbf{a_p}$. We assume these a priori scales have an isotropic uncertainty, $\mathbf{P}$, of 200 km.
2. Making a prior guess based on the local correlation with an uncertainty of 200 km ensures that the structure closest to the analysis point is influential in setting the calculated shape. It is one way to downweight the influence of spurious correlations that arise at far off locales. The other way we build localization into the method is through an uncertainty map, $\mathbf{R}$, for the correlation values defined as 1.01 minus the a priori Gaussian field. This states that we assume a signal to noise ratio of 0.01^{-2} at the point itself and of 1.01^{-2} as the distance from the point goes to infinity, and thus that we trust the local correlation values as much as 10^4 times more than the remote ones. If we do not implement $\mathbf{a_p}$, $\mathbf{P}$, and this structure in $\mathbf{R}$, we find that we are not able to fit the local correlation field with a Gaussian structure.
3. We estimate the Gaussian parameters, $\mathbf{a}$, using a least squares fit (e.g., Wunsch, 2006) of the form:

$$\mathbf{a}=\mathbf{a_p}+(\mathbf{H}^T\mathbf{R}^{-1}\mathbf{H}+\mathbf{P}^{-1})^{-1}\mathbf{H}^T\mathbf{R}^{-1}(\mathbf{y}-\mathbf{Ha_p}). \quad (1)$$

To orient the reader, if we were doing a simple least squares fit with no weighting (i.e., $\mathbf{R}=1$) and no a priori guess (i.e., $\mathbf{a_p}=0$ and $\mathbf{P}$ is infinite), we would obtain the conventional least squares solution: $\mathbf{a}=(\mathbf{H}^T\mathbf{H})^{-1}\mathbf{H}^T\mathbf{y}$. Adding the weighting and a priori guess is vital to limit the influence of spurious remote correlations.

4. We then do a principal axis rotation, solving for $(-a_1x^2-a_2xy-a_3y^2)=(-\alpha_1x'^2-\alpha_2y'^2)$ revealing the orientation of the Gaussian and the length-scales of the semimajor and semiminor axes.

The residuals from the fit are small, with the fit typically explaining over 90% of the weighted variance. Poor fits are found in a small number of locations near the coast, except for low-pass-filtered SST for which poor fits are found in some noncoastal regions, most notably in the subtropics. This is because the annual cycle is the dominant mode of variability in these regions and the local structure is not well represented by a Gaussian functional form. We do not remove the annual cycle from the low-pass SST time series; however, as this is a primary component of the system we wish to quantify. Moreover, the Gaussian fit does capture much of the local correlation structure over the majority of the domain. Thus, we analyze the entire domain, but with the caveat that for low-pass SST the separation of a local Gaussian correlation and a domain-wide annual cycle is unclear, leading to heightened uncertainty in quantification of *e*-folding scales in some regions. Regardless, a primary purpose of this calculation is to determine whether the correlation scales of the model are reasonable when compared with a different SST product, and we find this issue occurs in both analyses.

The resulting correlation scale maps are smooth, implying that we are not missing structure, and justifying the subsampling utilized. We do, however, find occasional single pixel outliers in our derived correlation scale maps. These outliers are both shorter and longer than surrounding pixels, and no bias is apparent. Inconsistency in the maps, manifest as abrupt changes in correlation scales, render the scales problematic for use in mapping. To ensure a level of smoothness we apply a median filter with adjacent pixels. Thus, the maps presented and used below represent the median value calculated in a 9° longitude by approximately 3.3° latitude box.

The orientations of the semimajor axes of the correlations are expected to be zonal. Indeed, for high-pass and low-pass SST and SSH fields, the correlations are either isotropic or oriented zonally over almost the entire domain (not shown). In the Antarctic and some regions of the ACC the principal axes are displaced from zonal, but nowhere are they truly meridional. For SSH, only 0.9% of the AVISO angles are greater than 15° and only 0.1% are greater than 45°. For B-SOSE, 7.8% of the points have angles greater than 15° and 1.0% have angles greater than 45°. For SST, 14.6% of the MWOI angles are greater than 15° and 2.3% are greater than 45°. For B-SOSE, 12.9% of the points have angles greater than 15° and only 0.4% have angles greater than 45°. Our findings suggest that the primary effect of meridional flow (e.g., in boundary currents) is to modulate the scales into an isotropic orientation. Thus, for simplicity we will refer to the semimajor axis as zonal and the semiminor axis as meridional throughout the rest of this text.

Because most of the SSH and SST variance is in the low-pass components, these are the most important scales to reproduce. In other words, high-pass SSH and SST are less representative of the full signal that one wishes to estimate. The zonal and meridional correlation scales for the low-pass components are qualitatively similar between the observationally derived products and B-SOSE (Figure 3). In general, the scales are shortest in the subpolar gyres and longest in the subtropics. There are some interesting exceptions, for example a location of long zonal correlation lengths in the in the eastern Weddell Sea, and shorter correlations found just north of the ACC below Africa and in the central Pacific sector.

Though the fields show structure in the zonal direction, to more easily quantify the differences we present the zonally averaged scales in Figure 4. (As can be seen in Figures 3 and 4, there is a strong meridional gradient in the length scales, making the meridionally averaged scales difficult to interpret, and we have chosen to not show it.) Plotting the ratio of zonally averaged scales for the observational products and B-SOSE shows that B-SOSE overestimates correlation scales by about 20% at most latitudes. The ratio is never more than 1.5, with the exception of the zonal scales of low-pass SSH, which are estimated to be more than twice as long in some regions of the ACC and the polar gyres (Figure 5). This largely arises from the fact that the B-SOSE ACC has much less high-wavenumber structure than the observational product. One could argue, however, that a dynamical mapping would follow streamlines, and solving for the Gaussian structure in a streamline coordinate system may lengthen the scales derived for the SSH product and bring these two estimates closer to consistency. For all other fields the ratios are relatively constant in latitude, implying that despite a bias toward overestimation, B-SOSE is able to capture much of the correlation scale structure.

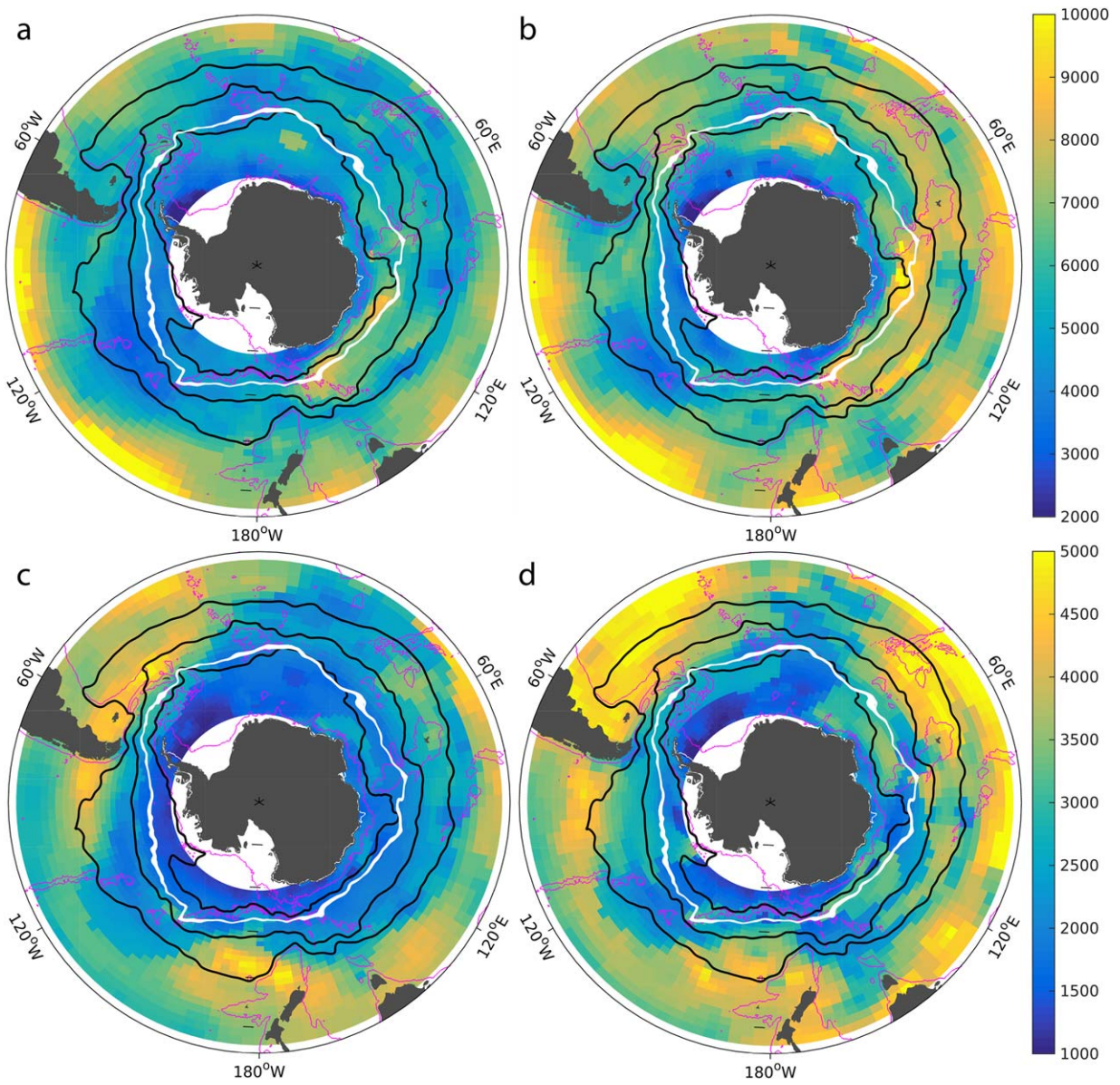

Figure 3. Correlation length scales for low-pass SST. Zonal scales from (a) MWOI observational product and (b) B-SOSE. Meridional scales from (c) MWOI observational product and (d) B-SOSE. As in Figure 1, the black contours are ACC streamlines, the white contour is mean August ice extent, and magenta is the 3,000 m bathymetric contour.

In the next section, we repeat the analysis to estimate the correlation lengths of quantities that are not directly measured by satellite: air-sea exchanges and inventories of carbon and heat. The length scales of heat fluxes are expected to be similar to those of SST due to the rapid equilibration of SST with the atmosphere. Carbon exchanges, which occur via CO_2 equilibration, occur on timescales typically longer than those of ocean vertical mixing (Williams & Follows, 2011). Therefore air-sea carbon exchanges and carbon and heat inventory will be more reflective of near surface ocean circulation, and therefore of the scales of SSH. The SSH and SST validation presented here suggests that the B-SOSE correlation scales are qualitatively accurate. We hypothesize that they are likely an overestimate of about 20% for the low-pass fields and about 30% for the high-pass fields, and consider this when drawing conclusions. Nevertheless, the large overestimate of the zonal low-pass SSH scales in parts of the ACC and the subpolar gyres (Figures 4a and 5b) cautions that there may be locations where the reported scales are greatly overestimated.

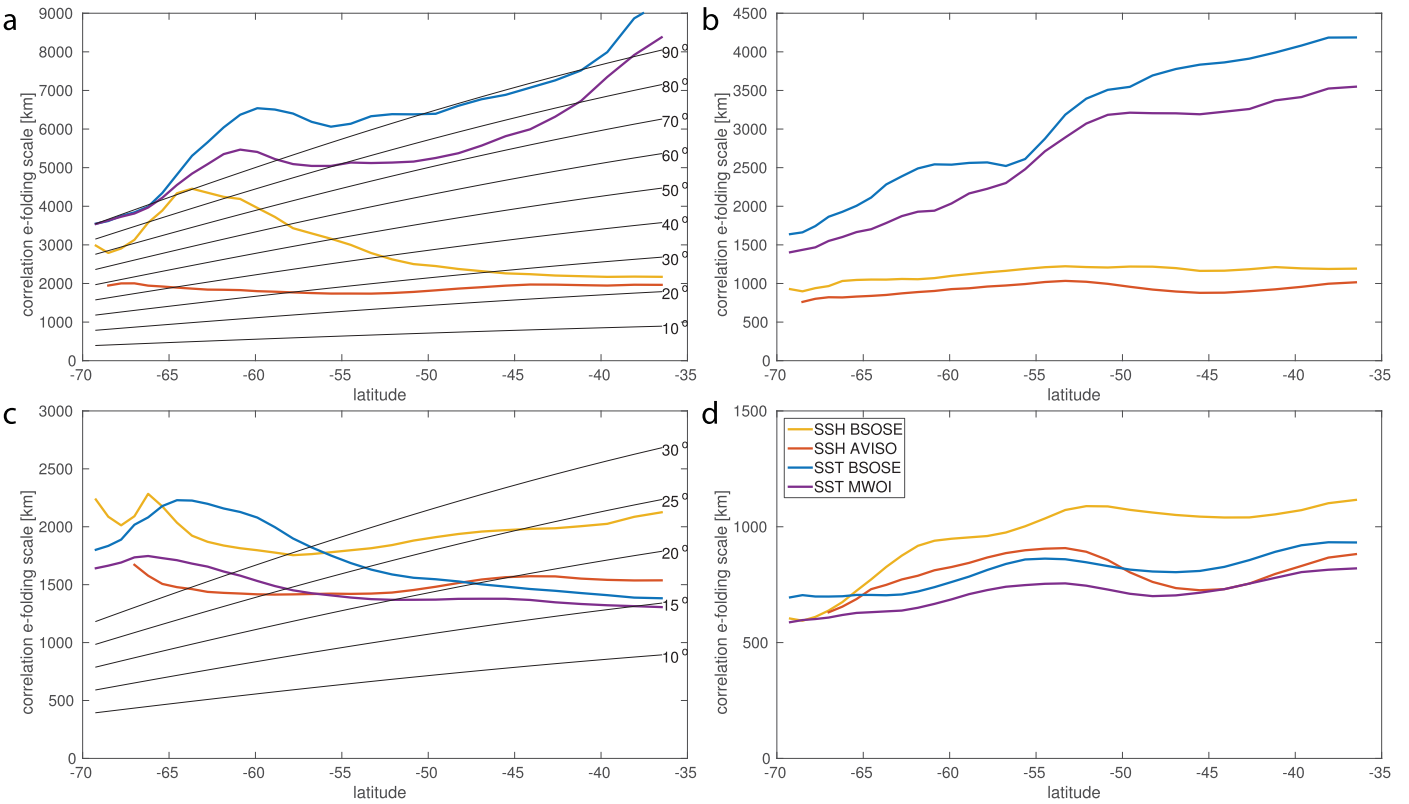

Figure 4. Zonally averaged correlation length scales for SST and SSH from observational products and from B-SOSE. (a) Low-pass zonal scales, (b) low-pass meridional scales, (c) high-pass zonal scales, and (d) high-pass meridional scales. Black lines approximately convert distance in km to degrees of longitude.

3. Results

3.1. Mean State and Temporal Variability of Carbon and Heat

In general, over the upper 950 m, integrated ocean heat content and average carbon content both change monotonically with latitude, but with heat increasing northward from Antarctica and with carbon decreasing northward (Figures 6c and 6d). The carbon fluxes largely reflect ocean vertical transport (Figure 6a). Carbon-rich waters are brought to the surface in and poleward of the Antarctic Circumpolar Current (ACC), and outgassing (positive flux) occurs in these latitudes. North of the ACC, water is subducted, allowing for carbon uptake. Departures from this background pattern are due to biological productivity acting as a

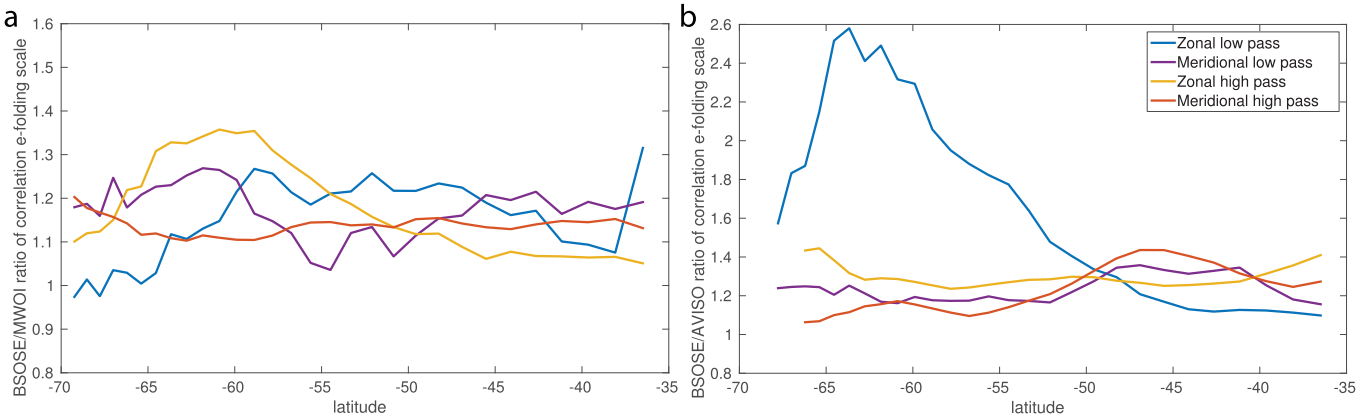

Figure 5. Correlation length-scale ratios for (a) SST and (b) SSH: B-SOSE scales divided by the observational product scales.

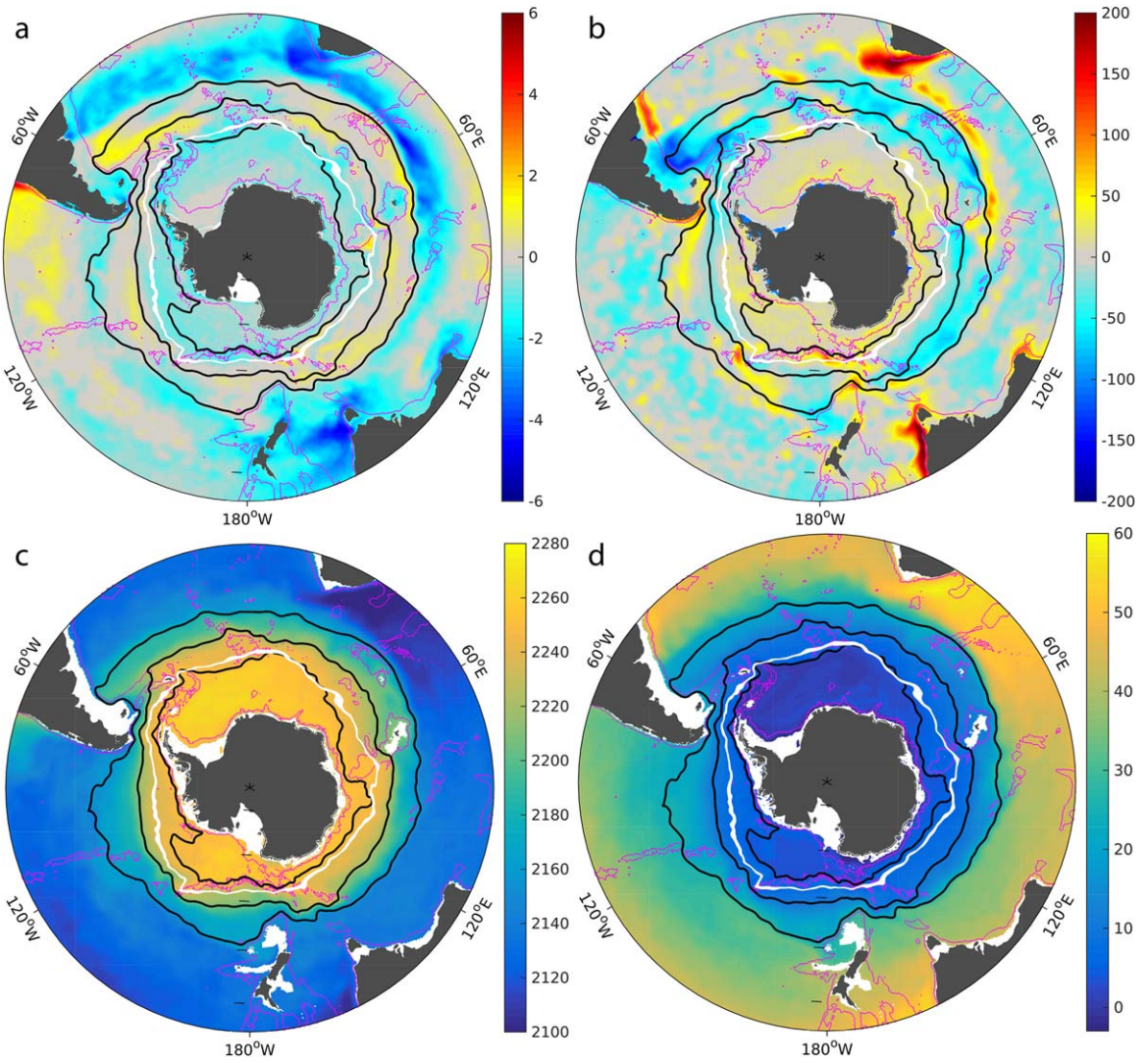

Figure 6. Mean fluxes from ocean to atmosphere of (a) carbon (mol m^{-2} yr^{-1}) and (b) heat (W m^{-2}), and upper 950 m, (c) average carbon content (μmol kg^{-1}), and (d) integrated heat inventory (GJ m^{-2}) from B-SOSE. As in Figure 1, the black contours are ACC streamlines, the white contour is mean August ice extent, and magenta is the 3,000 m bathymetric contour.

carbon sink or due to locations of strong currents, as shown in the B-SOSE carbon budget analysis carried out in Rosso et al. (2017). The mean heat flux is large wherever the circulation is meridionally steered by bathymetry (Figure 6b). The ocean gains heat (a negative flux following the convention that upward heat transport to the atmosphere is positive) where there is upwelling or where cold currents move equatorward (e.g., the Malvinas Current), and the ocean loses heat where warm currents move poleward (e.g., the Brazil Current). For more on the Southern Ocean air-sea heat fluxes see Tamsitt et al. (2016).

The standard deviations of the carbon flux and the upper 950 m average carbon content have similar qualitative structures (Figures 7a and 7c). Enhanced variability is apparent at strong ocean fronts (e.g., the Brazil-Malvinas Confluence) and in biologically productive regions (e.g., near Tasmania). Similarly, the standard deviations of heat flux and upper 950 m heat content also have the same qualitative features (Figures 7b and 7d) reflecting the frontal features of the ocean circulation. Heat flux is notably damped in the seasonally sea ice-covered region, while this is not the case for carbon. However, in the southwestern Weddell Sea, where ice is almost always present, the fluxes of both carbon and heat are negligible.

To illustrate the temporal structure of carbon, carbon flux, heat, and heat flux, we calculate the power spectral density at all model grid points poleward of 30°S and then average them together (Figure 8). The

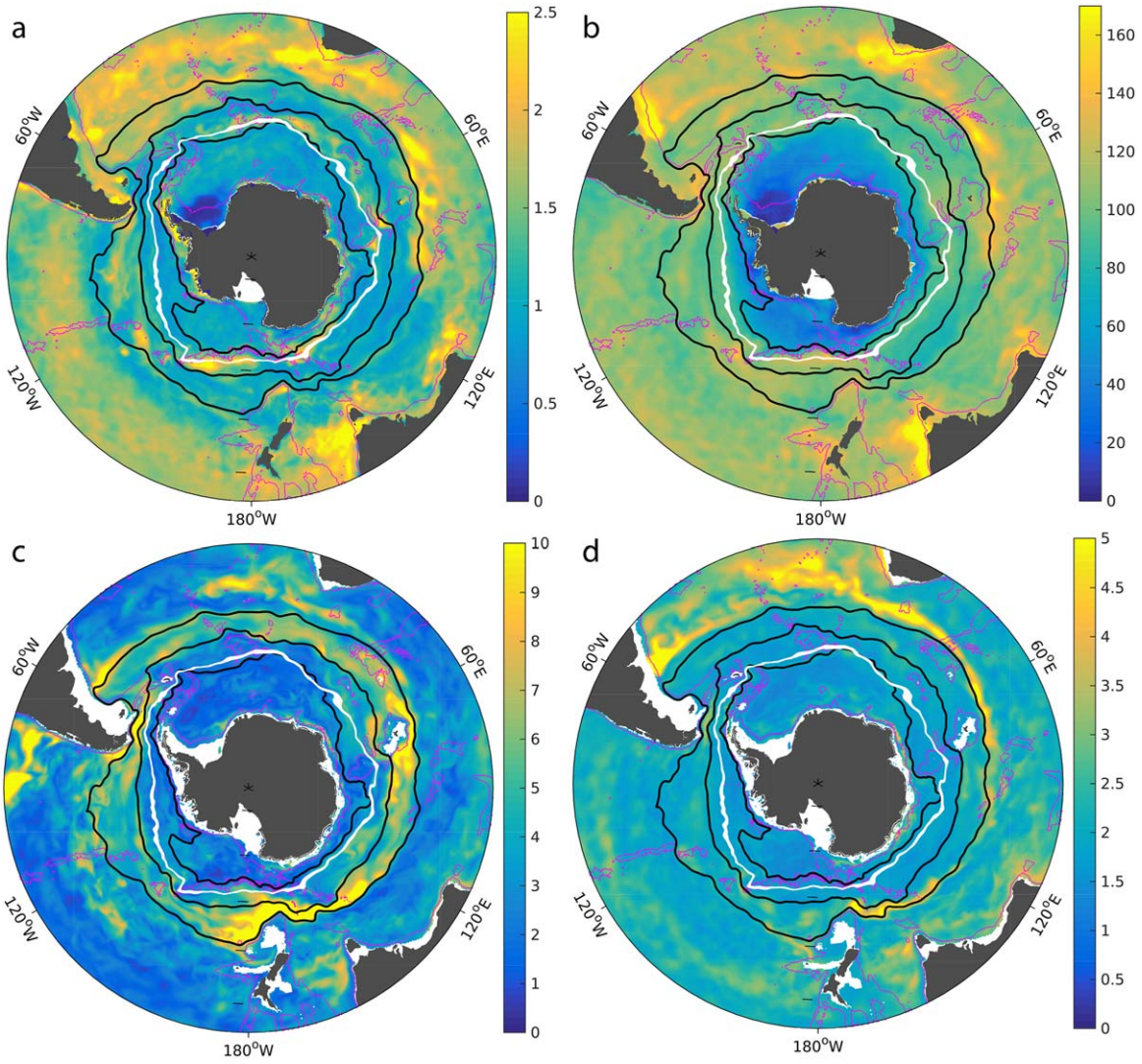

Figure 7. Standard deviation of fluxes of (a) carbon (mol m^{-2} yr^{-1}) and (b) heat (W m^{-2}), and standard deviation of upper 950 m, (c) average carbon content (μmol kg^{-1}), and (d) integrated heat inventory (GJ m^{-2}) from B-SOSE. As in Figure 1, the black contours are ACC streamlines, the white contour is mean August ice extent, and magenta is the 3,000 m bathymetric contour.

carbon and heat flux variances are dominated by the annual cycle and harmonics. The phase of the heat flux annual cycle is aligned with the sun, with the maximum at the austral summer solstice (i.e., ∼21 December; not shown). The peak amplitude in carbon flux annual cycle is shifted by about 51 days to ∼10 February. For the upper 950 m average carbon content and heat inventory fields, the annual cycle, and its harmonics are noteworthy, but less significant than for the fluxes. As expected, all fields have red spectra with most spectral power found above 90 days. The inventories, however, have a much steeper slope than the fluxes as expected from the integral relation between them.

As was done for SST and SSH, we calculate a low-pass component using a 90 day running mean and a high-pass component that is the orthogonal component of the residual. The low-pass components of carbon and heat flux explain 60 ± 12% and 69 ± 13% of the variance, respectively (Figure 9). The carbon flux shows far more ocean structure, especially around complex bathymetry and the ACC fronts, than the heat flux due to the slower equilibration time of CO_2 exchange between the atmosphere and ocean. The high-pass components of carbon and heat flux explain 39 ± 12% and 30 ± 13% of the variance, respectively. Only the low-pass components are shown, but one can infer the high-pass structure since the combination of the low-pass and high-pass components explains approximately 100% of the variance. Like carbon

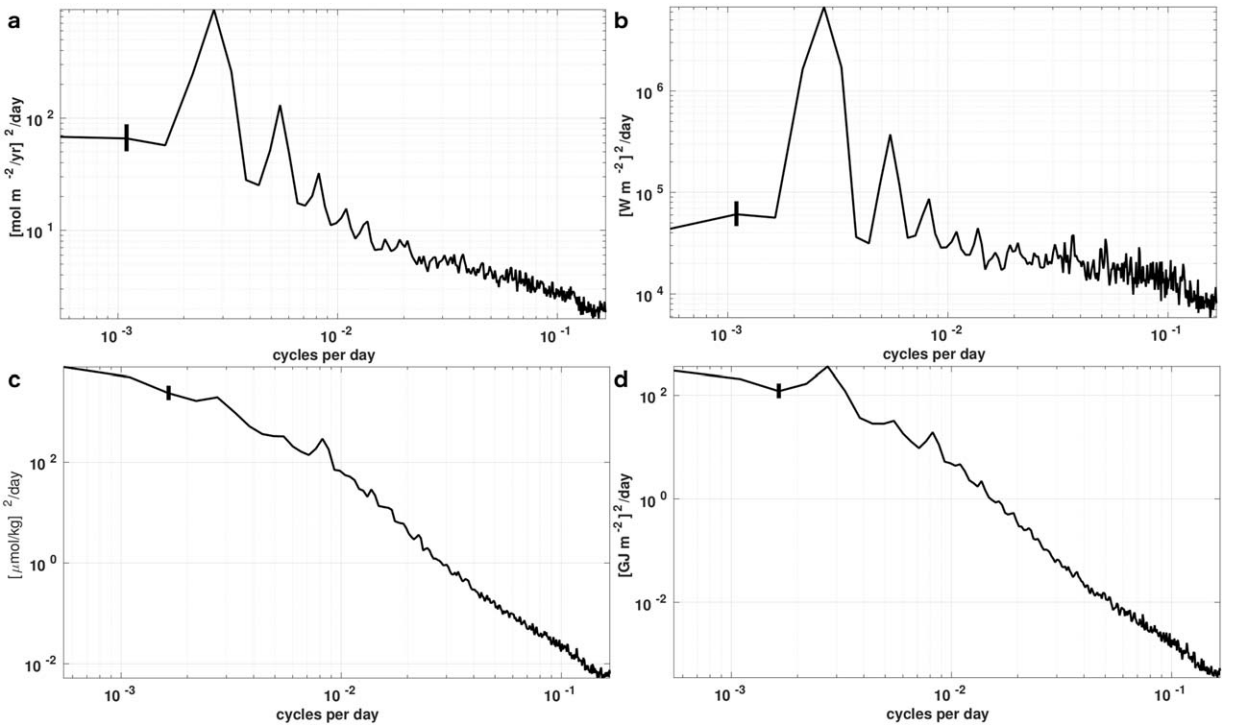

Figure 8. Power spectral density for (a) carbon flux, (b) heat flux, (c) upper 950 m average carbon content, and (d) upper 950 m integrated heat inventory. Error bars use the correlation scales diagnosed below for the low-pass components, and can be found in Table 1: the number of degrees of freedom assumed is 62 for carbon flux, 11 for heat flux, 98 for carbon content, and 70 for heat content.

flux, the decomposition between high and low-pass components of the carbon content reflects ocean structures, and the ACC fronts in particular. However, for inventory the low-pass components are far more dominant, explaining $96 \pm 4\%$ and $90 \pm 5\%$ of the variance for carbon and heat, respectively. This enhanced dominance of the low-pass components is expected given the steeper slope of the spectra for inventories (Figure 8).

3.2. Spatial Correlation Lengths of Carbon and Heat

The plots of variance explained show that the low-pass components are the most important fields to estimate. The low-pass components of carbon flux show long zonal correlation lengths reaching 7,000 km in the subtropics (Figure 10a). They reach a minimum of around 2,000 km in the ACC, with the exception being just upstream and downstream of the Campbell Plateau, and also in Drake Passage. The zonal scales are somewhat larger, at about 4,000 km, in the subpolar gyres. Meanwhile the meridional scales are always shorter, and show a very different pattern with the longest scales being about 2,500 km in the core of the ACC, and dropping to 1,500 km equatorward of the ACC, and about 1,000 km poleward of the ACC (Figure 10b). The low-pass components of heat flux have correlation scales that are smooth in space, with the zonal scale typically around 10,000 km, but reaching far higher when the ACC is in the Atlantic Sector and dropping to a minimum of about 4,000 km poleward of the ACC (Figure 10c). The meridional scales show minimal zonal structure, and increase rather monotonically from about 1,000 km poleward of the ACC to 8,000 km by 35°S (Figure 10d).

There is more structure in the spatial correlation scales of low-pass components of carbon and heat inventory. The zonal scales of carbon content are longest (approximately 2,500 km) in the Southeast Indian Ocean and at the northern flank of the ACC upstream of Kerguelen Plateau, Campbell Plateau, and the Pacific-Antarctic Ridge (Figure 11a). The meridional scales show similar structure, with longer scales in the Southeast Indian Ocean, around Campbell and Kerguelen Plateaus, and upstream of the Pacific-Antarctic Ridge. The meridional scales are shortest poleward of the ACC, although longer scales are found at the southern flank of the ACC in the southwest Indian Ocean sector (Figure 11b). Similar structures are found in

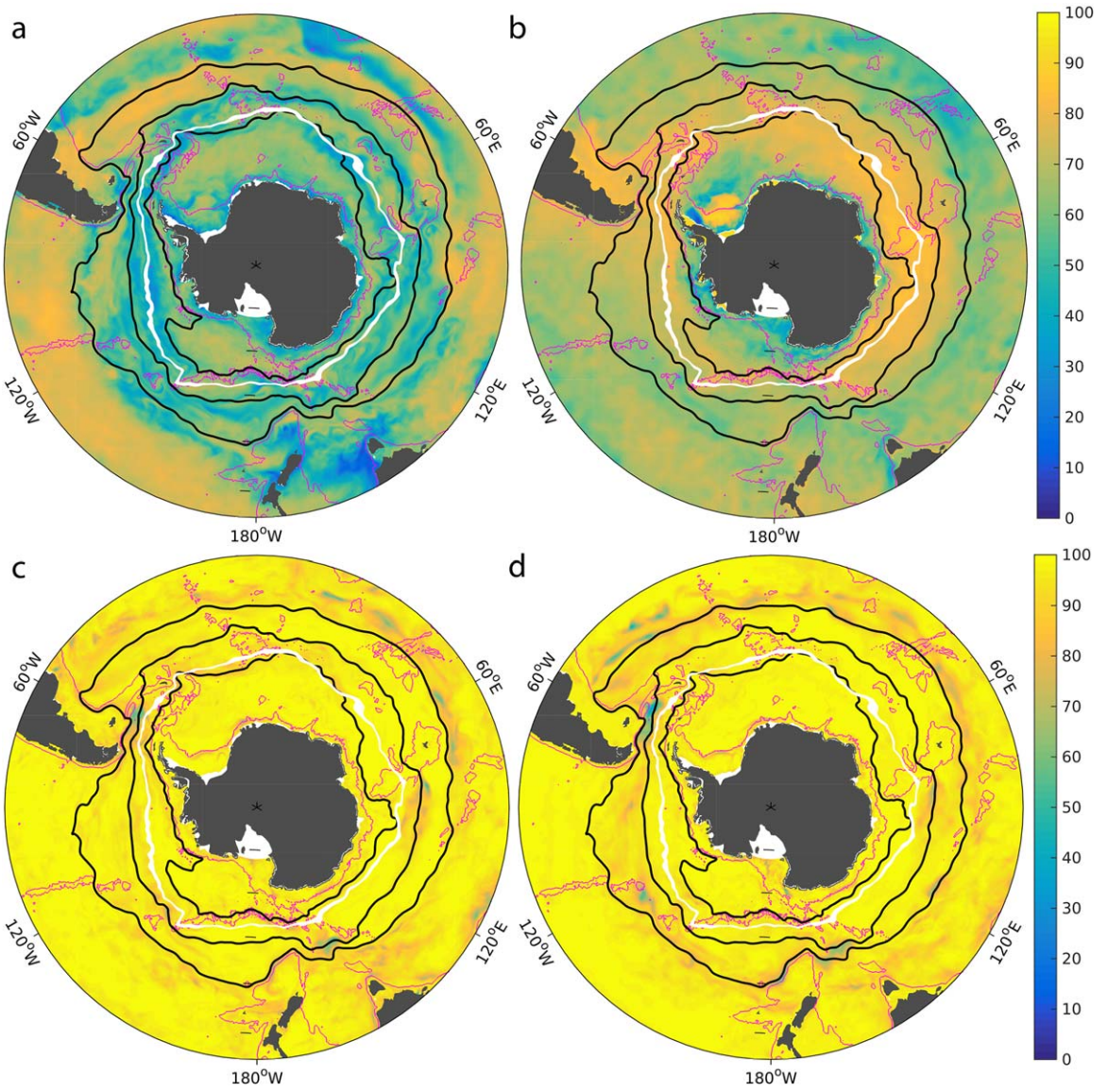

Figure 9. Percent variance explained by the low-pass components of (a) carbon flux, (b) heat flux, (c) upper 950 m average carbon content, and (d) upper 950 m integrated heat inventory. The high-pass components are not shown, but can be inferred as they account for the missing variance explained (i.e., low-pass + high-pass variance explained ≈ 100%). As in Figure 1, the black contours are ACC streamlines, the white contour is mean August ice extent, and magenta is the 3,000 m bathymetric contour.

the zonal component of heat inventory (Figure 11c), as were described in the zonal component of carbon content, though for heat content the Southeast Indian Ocean has shorter scales and the South Pacific Ocean has longer scales. The meridional correlation scales for heat inventory have the most structure, with scales changing from about 800 to 1,600 km in short distances (Figure 11d). This happens mostly around complex topography, but also in the South Indian Ocean.

Though variability is present in the spatial correlation scales, these fields are relatively smooth in space (Figures 10 and 11). Thus, zonal averaging is a reasonable way to summarize the results, which are shown as Figures 12a and 12b. The correlation scales of low-pass air-sea heat flux are found to be long, ranging from approximately 4,000 to 12,000 km in the zonal direction and 2,000 to 7,000 km in the meridional direction (Figures 10 and 12), largely due to the dominance of the annual cycle. The correlation scales for low-pass carbon and heat inventory are approximately 2,000 km in the zonal direction and 1,000 km in the meridional direction (Figure 11). They are relatively independent of latitude (Figures 12a and 12b). Air-sea carbon

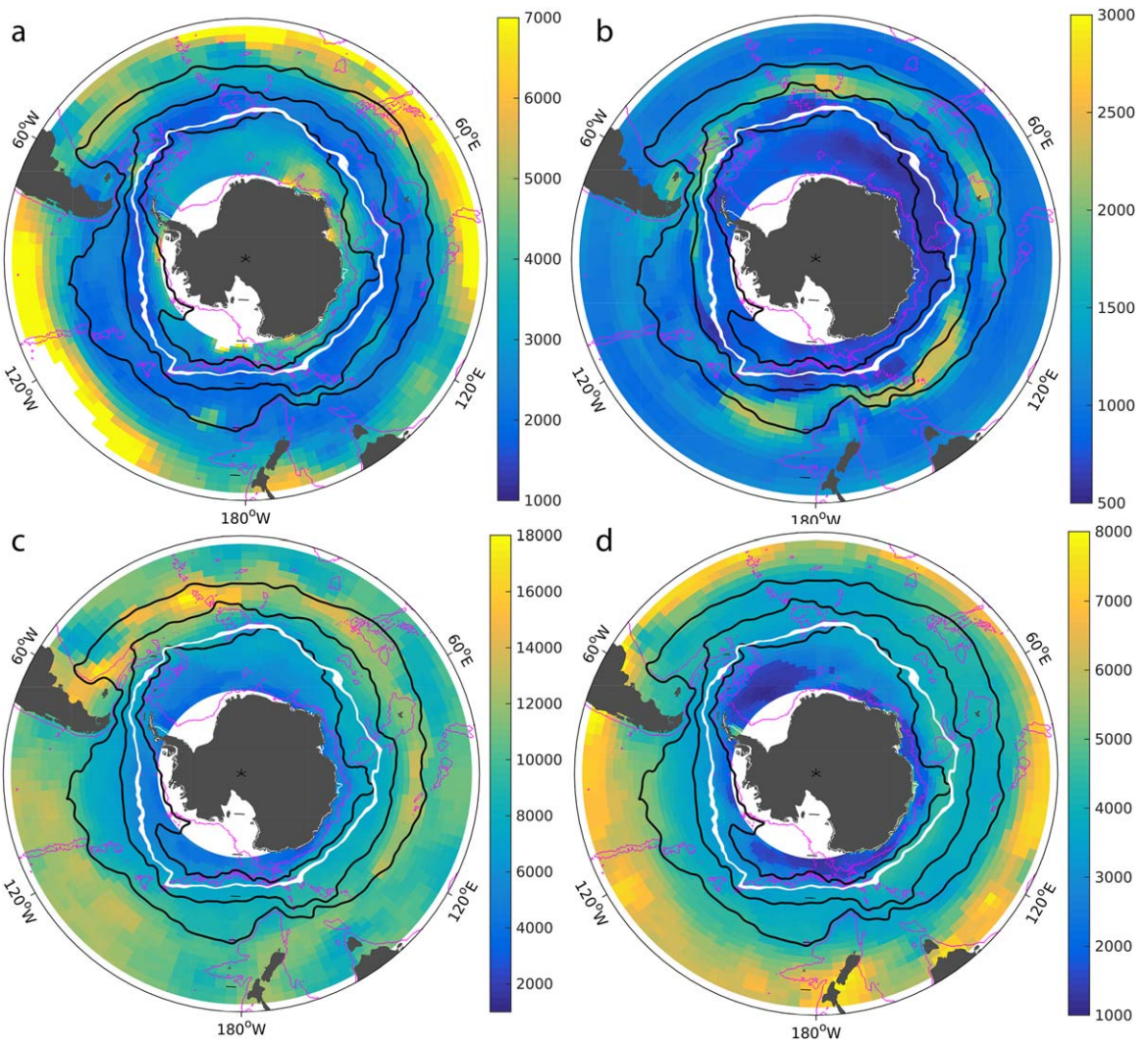

Figure 10. Correlation length scales (km) for low-pass components of carbon flux: (a) zonal scales and (b) meridional scales, and low-pass components of heat flux: (c) zonal scales and (d) meridional scales. As in Figure 1, the black contours are ACC streamlines, the white contour is mean August ice extent, and magenta is the 3,000 m bathymetric contour.

fluxes have length scales that are similar to the length scales of the inventory fields in the ACC latitudes, but the zonal scales become far longer in the subtropics.

We carry out an additional calculation considering the inventories integrated down to only 100 m instead of to 950 m (not shown). Integrating to this shallower depth potentially highlights the role of production. However, we find that the influence of the seasonal changes in mixing depth and ice formation are even more influential, obscuring the biological production signal. The resulting pattern thus primarily reflects physical changes and we do not show spatial maps. We do, however, show the zonal integrated correlation scales for low-pass carbon and heat inventory in the top 100 m in Figures 12a and 12b. Carbon inventory in this upper layer has significantly shorter scales than heat at all latitudes, reflecting the role of biology, and slower air-sea exchange in setting more high-wavenumber structure. The same story holds for the high-pass components, but again, even in the top 100 m the inventory signal is dominated by the low-pass components.

The zonally averaged high-pass scales are shown in Figures 12c and 12d. Here the fluxes have the shortest scales of about 1,300 km in the zonal direction and ranging from 500 to 900 km in the meridional direction. The inventories are similar, with a scale of approximately 1,600 km in the zonal direction and ranging from 600 to 1,000 km in the meridional direction.

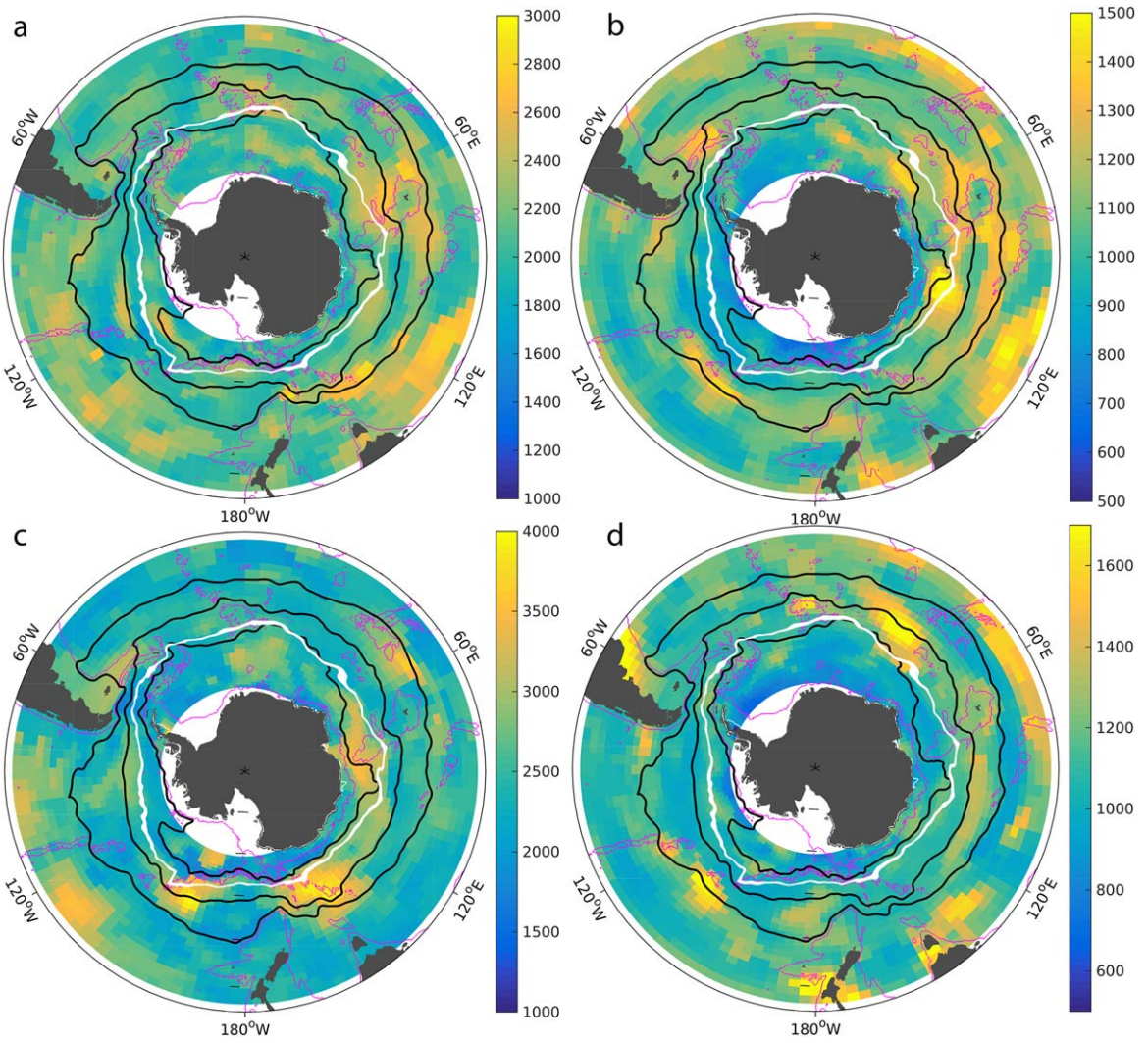

Figure 11. Correlation length scales (km) for low-pass components of upper 950 m average carbon content: (a) zonal scales and (b) meridional scales, and low-pass components of upper 950 m integrated heat inventory: (c) zonal scales and (d) meridional scales. As in Figure 1, the black contours are ACC streamlines, the white contour is mean August ice extent, and magenta is the 3,000 m bathymetric contour.

We summarize results in Table 1 for three regions: the subpolar, defined as 70°S–60°S; the ACC, defined as 60°S–45°S; and the subtropic, defined as 45°S–35°S. For these regions and for each property, we average the correlation scales and, as discussed in section 2.2, we scale by the factor determined from the ratio of model scales to the mapped products for SST and SSH. These scale factors represent bias due to the overly smooth model fields. The values range from about 1.1–2.2 for zonal scales and 1.1–1.4 for meridional scales. For each region, we use the approximate domain size to estimate the minimum number of floats necessary to constrain the field. This estimate assumes exactly one float per correlation length, and since perfect float distribution is impossible to attain, this is an underestimate. Nevertheless, it can be used to indicate minimum float requirements in each region: to meet the goal of estimating the large-scale Southern Ocean carbon content at least 98 floats are needed, distributed approximately uniformly through the three domains (about 36, 30, and 32 floats in the subpolar, ACC, and subtropic regions, respectively). This is slightly more than is needed for estimating the heat content. Far fewer floats are needed to estimate the spatial scales of the low-pass fluxes, but estimating these fields has the complication that the high-pass components explain at least a third of the variance. The number of floats required in excess of the numbers presented in Table 1 depends on both the need to resolve the temporal scales and the fact that floats will converge and maintaining a truly optimal coverage is unrealistic.

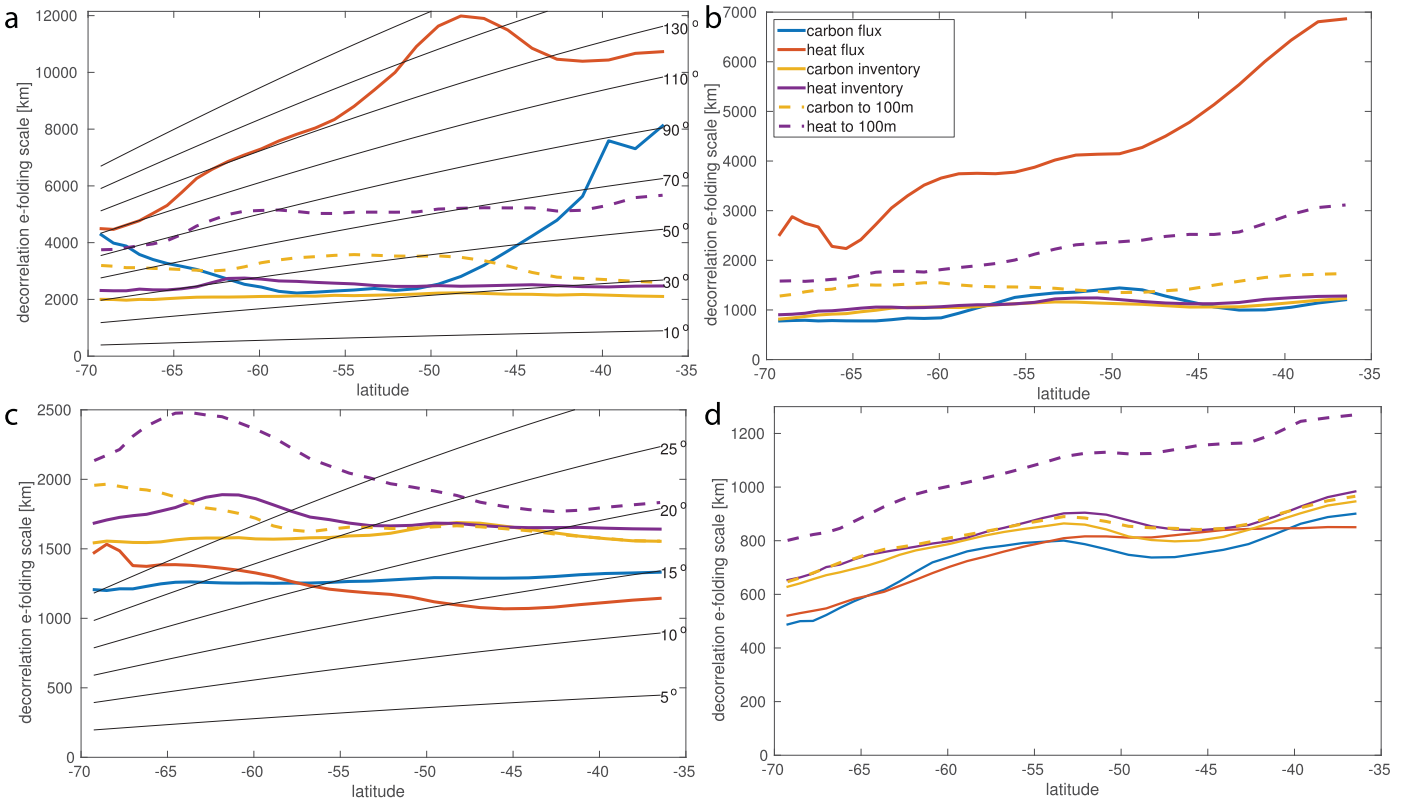

Figure 12. Zonal average of correlation length scales (km) for low-pass components: (a) zonal scales and (b) meridional scales, and also for high-pass components: (c) zonal scales and (d) meridional scales. Black lines approximately convert distance in km to degrees of longitude.

Table 1
Average Zonal and Meridional Correlation Length Scales for a Given Property

		Subpolar: 70°S–60°S		ACC: 60°S–45°S		Subtropic: 45°S–35°S		
		Correlation scale (km)	Floats required	Correlation scale (km)	Floats required	Correlation scale (km)	Floats required	Minimum floats 70°S–35°S
C inv LP	Zonal	1,062	16	1,457	15	1,922	16	94
	Mrdnl	784	2	905	2	900	2	
C inv HP	Zonal	1,171	15	1,283	17	1,213	25	131
	Mrdnl	648	2	672	3	669	2	
H inv LP	Zonal	1,272	14	1,691	13	2,213	14	68
	Mrdnl	827	2	946	2	966	1	
H inv HP	Zonal	1,344	13	1,333	17	1,259	24	125
	Mrdnl	672	2	702	3	689	2	
C flx LP	Zonal	1,624	11	1,724	13	4,374	7	62
	Mrdnl	657	2	1,041	2	856	2	
C flx HP	Zonal	922	19	1,006	22	1,004	30	164
	Mrdnl	541	2	624	3	634	2	
H flx LP	Zonal	4,999	4	8,207	3	9,405	4	11
	Mrdnl	2,251	1	3,673	1	5,149	1	
H flx HP	Zonal	1,098	16	992	22	1,039	29	156
	Mrdnl	519	2	702	3	743	2	

Note. The correlation scales and number of floats are derived after correcting for model biases using the correlation length scale ratios between the model and observational satellite products (Figure 5). A scaling based on SSH is used for inventories and carbon flux as these tend to have ocean scales. A scaling based on SST is used for heat flux. The correlation scales are combined with the size of the domain to estimate the minimum floats required to estimate the field with skill. This estimate assumes perfect float distribution (i.e., exactly one per correlation length). Abbreviations used in the table are C for carbon, H for heat, LP for low-pass, HP for high-pass, inv for inventory, flx for flux, and mrdnl for meridional.

3.3. Estimating the Ability of the Argo Array to Estimate Heat Inventory

As a practical example of the information provided, we use the derived spatial correlation scales of heat inventory (Figures 11c and 11d) to determine formal mapping skill from the Argo array positions. We implement the SSH correlation scale calibration adjustment shown in Figure 5b, such that scales being used are consistent with those given in Table 1. Since 2006, Argo has maintained over 600 floats poleward of 35°S. The density peaked with over 900 floats in 2010, and the array is currently maintaining over 700 floats in the region. In 2014, each month had between 561 and 621 unique floats reporting profiles flagged as good. (We include floats with interpolated positions.) April 2014 had 621 floats reporting good profiles. As an example data set, we take their last position of the month. We then estimate the variance that can be explained by these floats by constructing the data-data covariance, $\mathbf{C_{dd}}$, and model-data covariance matrix $\mathbf{C_{md}}$, and taking the diagonal of $\mathbf{C_{md}}\mathbf{C_{dd}}^{-1}\mathbf{C'_{md}}$ (e.g., Bretherton et al., 1976; Gille, 2003; Wunsch, 2006). Recognizing that the mapping omits high-wavenumber and high-frequency signals in the point samples, we must prescribe a representation error for each float measurement to account for that variance. As a first guess, we assume that 67% of the variance in a single measurement is due to signals other than the climate scales of variability we are seeking to estimate, and prescribe a signal to noise of 1/3 in estimating the mapping skill. Thus, we assume 2/3 of the variance in an Argo time series represents signals with periods less than 20 days or length-scales shorter than the approximately 1,000 km meridional and 2,000 km zonal scales that we use for mapping. Thorough analyses of representation errors from mapping methods, for example as discussed by Verdy et al. (2017) and Rödenbeck et al. (2015), are beyond the scope of this work, and the exercise we carry out here is simply a starting point yielding an example of the utility of this work.

The resulting estimate of formal mapping skill (Figure 13) has a value of 100% where the low-pass components of heat inventory are fully constrained, and a value of 0% where we estimate no skill. The root-mean-square of the variance explained is 76% between 35°S and 70°S. The variance explained is 81% equatorward

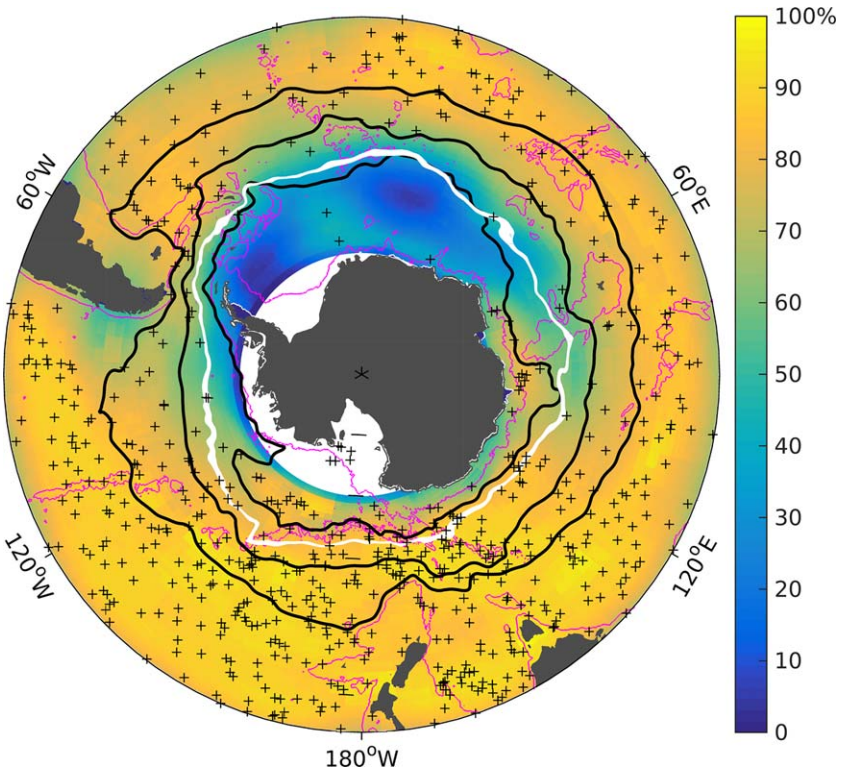

Figure 13. Estimate of formal mapping variance explained using the spatial correlation scales of heat inventory (Figures 11c and 11d) with the SSH bias correction (Figure 5b) and the 621 Argo float positions from April 2014. A signal to noise of 1/3 is prescribed. A value of 100% implies the low-pass heat inventory signal is fully constrained, while a value of 0% implies no information is provided by the array.

of the seasonally ice-covered region, with this region denoted by white lines in the figures. This supports the value of published inferences of heat changes from mapped Argo (e.g., Roemmich et al., 2015). When considering the region between the ice extent contour and 70°S the skill drops to 53% due to the lack of constraints in the subpolar gyres. This will improve, however, as floats with ice-avoidance software are now being deployed in these regions more often.

4. Conclusions

We have presented a method for estimating correlation scales from a model solution, and used the method to quantify scales from a biogeochemical state estimate. As illustrated in Table 1, the derived scales can be used to estimate observational requirements. As illustrated in section 3.3, these scales can also be used for statistical mapping of the properties, and to infer uncertainty in mapped products.

We have shown both similarities and differences between correlation scales of properties. Regarding temporal scales derived using our 3 day average model output, we find that inventories, which integrate fluxes, are dominated by variability with periods longer than 90 days. The majority of the flux temporal variability also occurs on periods longer than 90 days, but the high-pass flux components are also significant, explaining approximately a third of the variance. Spatial scales of carbon and heat inventory are similar, but the specific structure varies. Furthermore, carbon scales are always slightly shorter, and this discrepancy is even greater near the surface. This shortening of the scales is likely a combination of the influence of biology and the slower equilibration time of carbon with the atmosphere. Also, due to the slower equilibration time, we find carbon fluxes have scales similar to inventories in the ACC, but far longer in the subtropics. Low-pass heat fluxes have by far the longest correlation scales.

There are important assumptions that go into a calculation of this nature. The largest caveat is that we infer these statistics from a $1/3^{\circ}$ state estimate, B-SOSE. The B-SOSE resolution damps small-scale physics and overestimates the importance of low wavenumber scales. B-SOSE is data assimilating, and thus observations can provide some high-wavenumber structure, but observations are rather sparse and the state estimate is constructed to leave out ambiguous structure. We expect the model's high-wavenumber structure is attenuated relative to reality. In an attempt to correct for this bias, we have validated the statistics against observational products. The length-scale bias corrections calculated for SST and SSH were applied to our float requirement estimates. However, these SST and SSH products may also overestimate the true correlation scales. Future work will refine or validate the scales we have inferred via comparison to other mapped products, model solutions, or with data as the observational array becomes more extensive.

Quantifying correlation scales and providing Table 1 guides the minimum required float array size. Limitations in the ability of observations to represent the large scales we wish to estimate mean that the numbers given in the table are a lower bound. Argo's standard 10 day sampling may be adequate to beat down the noise for trends in dissolved inorganic carbon inventory, as this field varies relatively slowly. However, this sampling will be inadequate for carbon fluxes (Monteiro et al., 2015), implying a need for more floats than indicated in Table 1. One may envision that moorings spaced a correlation scale apart would be able to capture all time scales, but this observing system may still be susceptible to aliasing high-wavenumber structure. Even 94 moorings may be a lower bound for estimating the low-pass components of Southern Ocean carbon inventory. Improving our understanding of property variance in frequency and wavenumber space is vital for understanding error structure in derived maps. High-wavenumber variance is less significant in B-SOSE, but determining the structure of the true signal is necessary to inform the representativeness of measurements to the larger scales. Future work should apply the method presented to higher resolution models to refine the estimates of high-pass variance and to determine the influence of small-scale physics on low-wavenumber properties.

Another significant caveat regarding the array requirements presented in Table 1 is the assumption that each float accurately constrains the desired property. While floats are capable of estimating heat inventory, current sensor limitations mean that floats do not measure carbon content, carbon flux, or heat flux, but instead must infer these quantities, incurring nonnegligible error (Williams et al., 2017). Thus, beyond the aliasing representation error component discussed above, for some properties we must also consider additional representation error due to instrument limitations. For these properties, even more observations are needed in order to raise the signal above the noise.

In practice float measurements have uncertainty in representing climate-scale signals. Furthermore, the array cannot be expected to achieve optimal spacing due to deployment opportunity limitations and the lack of controllability of individual trajectories. As a demonstration of the utility of these scales for informing the level to which a property is constrained, and also to demonstrate the degree to which the minimum float requirement may be an underestimate we have assessed mapping uncertainty of heat content. We use the inferred correlation scales to estimate that the April 2014 Argo array of 621 floats was able to resolve approximately 75% of the climate-scale ocean heat content change signal. Whether resolving 75% of the signal is adequate depends on accuracy requirements. This emphasizes, however, that though only approximately 68 platforms are required to obtain one record per correlation scale, if we wish to fully constrain the signal, we also must understand and account for error in mapping, and for this purpose even an array of ∼600 floats is imperfect. The Southern Ocean heat inventory is clearly not overconstrained; there is room for improvement either by adding floats or possibly by achieving a more optimal float distribution.

Thus, significant representation error implies a need for more floats than indicated in the table. Nevertheless, there is reason to be optimistic that these error sources can be mitigated. The oceanographic community has sophisticated tools, like the state estimation software with which B-SOSE was produced, for constructing mapped products. These tools take into account covariance information. For example, measurements of oxygen and salinity will constrain inferences of carbon and heat content and fluxes. When one considers the entire observing system, which includes satellite measurements and moorings, it is possible that with optimized deployment the minimum float numbers given in Table 1 are actually reasonable for estimating climate variability. This is yet to be verified, but will become apparent as these mapping tools evolve and are better tested.

Acknowledgments
This work was sponsored by NSF's Southern Ocean Carbon and Climate Observations and Modeling (SOCCOM) Project under the NSF Award PLR-1425989. Logistical support for this project in Antarctica was provided by the U.S. National Science Foundation through the U.S. Antarctic Program. The 3 day average B-SOSE output used in this work is available at http://sose.ucsd.edu/BSOSE_iter105_solution.html. The SSH product was produced by CLS Space Oceanography Division and distributed by Aviso, with support from Cnes (http://www.aviso.altimetry.fr). The microwave OI SST data are produced by Remote Sensing Systems and sponsored by National Oceanographic Partnership Program (NOPP) and the NASA Earth Science Physical Oceanography Program. Data are available at www.remss.com. Argo data were collected and made freely available by the International Argo Program and the national programs that contribute to it. (http://www.argo.ucsd.edu, http://argo.jcommops.org, (http://doi.org/10.17882/42182). The Argo Program is part of the Global Ocean Observing System. This manuscript was improved by constructive criticism from two anonymous reviewers.

References

Abernathey, R. P., Cerovecki, I., Holland, P. R., Newsom, E., Mazloff, M., & Talley, L. D. (2016). Water-mass transformation by sea ice in the upper branch of the southern ocean overturning. *Nature Geoscience*, *9*(8), 596–601.

Bretherton, F. P., Davis, R. E., & Fandry, C. (1976). A technique for objective analysis and design of oceanographic experiments applied to mode-73. *Deep Sea Research and Oceanographic Abstracts*, 23, 559–582.

Chierici, M., Signorini, S. R., Mattsdotter-Bjork, M., Fransson, A., & Olsen, A. (2012). Surface water fCO_2 algorithms for the high-latitude Pacific sector of the Southern Ocean. *Remote Sensing of Environment*, *119*, 184–196.

Donohue, K. A., Tracey, K. L., Watts, D. R., Chidichimo, M. P., & Chereskin, T. K. (2016). Mean Antarctic circumpolar current transport measured in Drake passage. *Geophysical Research Letters*, *43*, 11760–11767. https://doi.org/10.1002/2016GL070319

Galbraith, E. D., Gnanadesikan, A., Dunne, J. P., & Hiscock, M. R. (2010). Regional impacts of iron-light colimitation in a global biogeochemical model. *Biogeosciences*, *7*, 1043–1064.

Garrett, C., & Munk, W. (1975). Space-time scales of internal waves: A progress report. *Journal of Geophysical Research*, *80*(3), 291–297. https://doi.org/10.1029/JC080i003p00291

Giering, R., & Kaminski, T. (1998). Recipes for adjoint code construction. *ACM Transactions on Mathematical Software*, *24*(4), 437–474.

Gilbert, J. C., & Lemaréchal, C. (1989). Some numerical experiments with variable-storage quasi-Newton algorithms. *Mathematical Programming*, *45*, 407–435.

Gille, S. T. (2003). Float observations of the Southern Ocean. Part I: Estimating mean fields, bottom velocities, and topographic steering. *Journal of Physical Oceanography*, *33*(6), 1167–1181. https://doi.org/10.1175/1520-0485(2003)033<1167:FOOTSO>2.0.CO;2

Johnson, K. S., & Claustre, H. (2016). Bringing biogeochemistry into the Argo age. *Eos*, *97*, 407–435. https://doi.org/10.1029/2016EO062427

Jones, S. D., Le Quere, C., & Rodenbeck, C. (2012). Autocorrelation characteristics of surface ocean pCO_2 and air-sea CO_2 fluxes. *Global Biogeochemical Cycles*, *26*, GB2042. https://doi.org/10.1029/2010GB004017

Landschutzer, P., Gruber, N., Bakker, D. C. E., & Schuster, U. (2014). Recent variability of the global ocean carbon sink. *Global Biogeochemical Cycles*, *28*, 927–949. https://doi.org/10.1002/2014GB004853

Losch, M., Menemenlis, D., Campin, J.-M., Heimbach, P., & Hill, C. (2010). On the formulation of sea-ice models. Part 1: Effects of different solver implementations and parameterizations. *Ocean Modelling*, *33*(1–2), 129–144.

Marshall, J., Adcroft, A., Hill, C., Perelman, L., & Heisey, C. (1997). A finite-volume, incompressible Navier-Stokes model for studies of the ocean on parallel computers. *Journal of Geophysical Research: Oceans*, *102*(C3), 5753–5766. https://doi.org/10.1029/96JC02775

Monteiro, P. M. S., Gregor, L., Lvy, M., Maenner, S., Sabine, C. L., & Swart, S. (2015). Intraseasonal variability linked to sampling alias in air-sea CO_2 fluxes in the Southern Ocean. *Geophysical Research Letters*, *42*, 8507–8514. https://doi.org/10.1002/2015GL066009

Purkey, S. G., & Johnson, G. C. (2010). Warming of global abyssal and deep Southern Ocean waters between the 1990s and 2000s: Contributions to global heat and sea level rise budgets. *Journal of Climate*, *23*(23), 6336–6351. https://doi.org/10.1175/2010JCLI3682.1

Riser, S. C., Freeland, H. J., Roemmich, D., Wijffels, S., Troisi, A., Belboch, M., et al. (2016). Fifteen years of ocean observations with the global Argo array. *Nature Climate Change*, *6*, 145–153. https://doi.org/10.1038/nclimate2872

Rödenbeck, C., Bakker, D. C. E., Gruber, N., Iida, Y., Jacobson, A. R., Jones, S., et al. (2015). Data-based estimates of the ocean carbon sink variability: First results of the surface ocean pCO_2 mapping intercomparison (SOCOM). *Biogeosciences*, *12*(23), 7251–7278. https://doi.org/10.5194/bg-12-7251-2015

Roemmich, D., Church, J., Gilson, J., Monselesan, D., Sutton, P., & Wijffels, S. (2015). Unabated planetary warming and its ocean structure since 2006. *Nature Climate Change*, *5*(3), 240–245.

Rosso, I., Mazloff, M. R., Verdy, A., & Talley, L. D. (2017). Space and time variability of the Southern Ocean carbon budget. *Journal of Geophysical Research: Oceans*, *122*, 7407–7432. https://doi.org/10.1002/2016JC012646

Russell, J. L., Dixon, K. W., Gnanadesikan, A., Stouffer, R. J., & Toggweiler, J. R. (2006). The southern hemisphere westerlies in a warming world: Propping open the door to the deep ocean. *Journal of Climate*, *19*(24), 6382–6390. https://doi.org/10.1175/JCLI3984.1

Swart, S., Thomalla, S., & Monteiro, P. (2015). The seasonal cycle of mixed layer dynamics and phytoplankton biomass in the sub-Antarctic zone: A high-resolution glider experiment. *Journal of Marine Systems*, *147*, 103–115. https://doi.org/10.1016/j.jmarsys.2014.06.002

Tamsitt, V., Talley, L. D., Mazloff, M. R., & Cerovečki, I. (2016). Zonal variations in the Southern Ocean heat budget. *Journal of Climate*, *29*(18), 6563–6579. https://doi.org/10.1175/JCLI-D-15-0630.1

Verdy, A., Cornuelle, B., Mazloff, M. R., & Rudnick, D. L. (2017). Estimation of the tropical Pacific Ocean state 2010–2013. *Journal of Atmospheric and Oceanic Technology*, *34*(7), 1501–1517. https://doi.org/10.1175/JTECH-D-16-0223.1

Verdy, A., & Mazloff, M. R. (2017). A data assimilating model for estimating Southern Ocean biogeochemistry. *Journal of Geophysical Research: Oceans*, *122*, 6968–6988. https://doi.org/10.1002/2016JC012650

Williams, N. L., Juranek, L. W., Feely, R. A., Johnson, K. S., Sarmiento, J. L., Talley, L. D., et al. (2017). Calculating surface ocean pCO_2 from biogeochemical Argo floats equipped with pH: An uncertainty analysis. *Global Biogeochemical Cycles*, *31*, 591–604. https://doi.org/10.1002/2016GB005541

Williams, R., & Follows, M. (2011). *Ocean dynamics and the carbon cycle: Principles and mechanisms*. Cambridge, UK: Cambridge University Press.

Wunsch, C. (2006). *Discrete inverse and state estimation problems: With geophysical fluid applications*. Cambridge, UK: Cambridge University Press.

Wunsch, C., & Heimbach, P. (2013). Chapter 21: Dynamically and kinematically consistent global ocean circulation and ice state estimates. In J. G. Gerold Siedler et al. (Eds.), *Ocean circulation and climate*, A 21st century perspective, international geophysics (Vol. 103, pp. 553–579). Cambridge, MA: Academic Press. https://doi.org/10.1016/B978-0-12-391851-2.00021-0